

Banner appropriate to article type will appear here in typeset article

Vortex Dynamics in Rotating Rayleigh-Bénard Convection

Shan-Shan Ding¹, Guang-Yu Ding^{2,3}, Kai Leong Chong^{3,4}, Wen-Tao Wu¹, Ke-Qing Xia^{2,3}† and Jin-Qiang Zhong^{1,5}‡

¹School of Physics Science and Engineering, Tongji University, Shanghai 200092, China

²Center for Complex Flows and Soft Matter Research and Department of Mechanics and Aerospace Engineering, Southern University of Science and Technology, Shenzhen 518055, China

³Department of Physics, The Chinese University of Hong Kong, Shatin, Hong Kong, China

⁴Shanghai Institute of Applied Mathematics and Mechanics, School of Mechanics and Engineering Science, Shanghai University, Shanghai 200072, China

⁵Department of Aeronautics and Astronautics, Fudan University, Shanghai 200433, China

(Received xx; revised xx; accepted xx)

We investigate the spatial distribution and dynamics of the vortices in rotating Rayleigh-Bénard convection in a reduced Rayleigh-number range $1.3 \leq Ra/Ra_c \leq 166$. Under slow rotations ($Ra \geq 10Ra_c$), the vortices are randomly distributed. The size-distribution of the Voronoi cells of the vortex centers is well described by the standard Γ distribution. In this flow regime the vortices exhibit Brownian-type horizontal motion. The probability density functions of the vortex displacements are, however, non-Gaussian at short time scales. At modest rotating rates ($4Ra_c \leq Ra \leq 10Ra_c$) the centrifugal force leads to radial vortex motions, i.e., warm cyclones (cold anticyclones) moving towards (outward from) the rotation axis. The mean-square-displacements of the vortices increase faster than linearly at large time. This super-diffusive behavior can be satisfactorily explained by a Langevin model incorporating the centrifugal force. In the rapidly rotating regime ($1.6Ra_c \leq Ra \leq 4Ra_c$) the vortices are densely distributed, with the size-distribution of their Voronoi cells differing significantly from the standard Γ distribution. The hydrodynamic interaction of neighboring vortices results in formation of vortex clusters. Inside clusters the correlation of the vortex velocity fluctuations is scale free, with the correlation length being approximately 30% of the cluster length. We examine the influence of cluster forming on the dynamics of individual vortex. Within clusters, cyclones exhibit inverse-centrifugal motion as they submit to the motion of strong anticyclones, while the velocity for outward motion of the anticyclones is increased. Our analysis show that the mobility of isolated vortices, scaled by their vorticity strength, is a simple power function of the Froude number.

Key words: rotating turbulence, turbulent convection, vortex dynamics, collective behavior

† Email address for correspondence: xiakq@sustech.edu.cn

‡ Email address for correspondence: jinqiang@fudan.edu.cn

1. Introduction

Buoyancy-driven convection is relevant to many natural flows in the atmosphere, oceans and planetary systems (Marschall & Scott 1999; Vallis 2006; Jones 2011). A rich variety of vortex structures arise during buoyant convection, especially in the presence of background rotations (Hopfinger & van Heijst 1993). Vortices are often referred to as coherent structures that consist of recirculating flows with roughly circular streamlines. The dynamics of vortices plays an important role in determining fluid motions and turbulent transport, ranging from small-scale turbulence to planetary-scale circulations (Fernando & Smith 2001). The dynamics convective vortices can be studied using a paradigmatic model, rotating Rayleigh-Bénard convection (RBC), i.e., a fluid layer heated from below and rotated about a vertical axis. In rotating RBC, the fluid flows are governed by a sets of non-dimensional parameters including the Rayleigh number (Ra) describing the strength of thermal forcing, the Ekman number (Ek) representing the rotating effect, the Froude number (Fr) for the strength of centrifugal force, the Prandtl number (Pr) for the fluid properties and the aspect ratio Γ_a describing the geometry of the fluid domain:

$$Ra = \frac{g\alpha\Delta TH^3}{\kappa\nu}, Ek = \frac{\nu}{2\Omega^2 H}, Fr = \frac{\Omega^2 D_0}{2g}, Pr = \frac{\nu}{\kappa}, \Gamma_a = D_0/H.$$

Here g denotes the gravity acceleration, ΔT is the applied temperature difference, D_0 and H are the horizontal and vertical length scales of the fluid domain, respectively. α , κ and ν are the thermal expansion, thermal diffusivity, and kinetic viscosity of the working fluid. Ω is the applied rotating velocity along a vertical axis.

A number of previous investigations report that for rapidly rotating RBC, the convective flows are organized by the Coriolis force into columnar vortices (Boubnov & Golitsyn 1986; Sakai 1997; Vorobieff & Ecke 2002; Portegies *et al.* 2008; King *et al.* 2009; Kunnen *et al.* 2010; Grooms *et al.* 2010; Julien *et al.* 2012; Shi *et al.* 2020). The formation of a columnar vortex can be described by the theory of thermal wind balance, which states that vertical velocity gradients is caused by horizontal temperature gradients in the flow field (Kundu & Cohen 2008)

$$2\Omega \frac{\partial \vec{u}}{\partial z} = -\alpha g \hat{e}_z \times \nabla T. \quad (1.1)$$

When observed in the lower fluid level, upwelling warm fluid elements rotate in the same direction as the system when they experience horizontal advection, forming cyclones. Oppositely, cold downwelling fluid elements are organized into anticyclones. Under thermal wind balance, the horizontal gradient in the right hand side of Eq. (1.1) alters the vertical velocity and vorticity in magnitude along vertical axis and their signs around the middle plane. Both types of vortices are tall, thin, coherent convection columns with their horizontal scale given by $l = (2\pi^4)^{1/6} Ek^{1/3} H$ for high-Pr fluids in the limit of rapid rotations (Chandrasekhar 1961; Julien & Knobloch 1998; Aurnou *et al.* 2018). The number density n of the columnar vortices increases when Ek decreases. It is found in previous studies that n can be described by a power-function of Ek , i.e., $n \propto Ek^{\gamma_n}$ (Boubnov & Golitsyn 1986; Sakai 1997; Vorobieff & Ecke 2002; Kunnen *et al.* 2010). Different scaling exponents γ_n varying from -1.5 to -0.4 are reported in these studies, which is presumably ascribed to the different fluid heights where measurements are made and the various criterion used to identify vortices. The mean spacing between the columnar vortices is given by $d_v \propto \sqrt{1/n}$ (Sakai 1997), assuming that the vortices are uniformly distributed. However, when the spatial distribution of the vortices are not uniform, as observed by Chong *et al.* (2020) and Ding *et al.* (2021) in

rapidly rotating RBC, the vortex spacing d_v is not simply a square-root function of n , then a more comprehensive description of the vortex spatial distribution is required.

The flow structure of the columnar vortices in rotating RBC was investigated in numerical simulation (Julien *et al.* 1996) and in laboratory experiments (Vorobieff & Ecke 1998). These studies discovered that each columnar vortex is surrounded by a shielding layer. The signs of vorticity, temperature anomaly and vertical velocity in the shield layer are opposite to that in the vortex core region. Portegies *et al.* (2008) proposed a theoretical model for the flow structures of the columnar vortices, in which they consider linearized governing equations of fluid motion and provide analytical solutions for the radial profiles of temperature fluctuations, vertical velocity and vorticity. An asymptotic theory of rapidly rotating RBC was developed by Sprague *et al.* (2006); Grooms *et al.* (2010), where they suggested that in the limit of extremely rapid rotations the columnar vortex structure is steady and axially and vertically symmetric, and predicted that the poloidal stream function of the vortices can be described by the zeroth-order Bessel function of the first kind (Grooms *et al.* 2010). It follows that both the radial profiles of the azimuthal velocity and the vertical vorticity can be expressed by prescribed Bessel functions. These predictions appeared to match with numerical simulations (Grooms *et al.* 2010; Nieves *et al.* 2014). Recently, Shi *et al.* (2020) performed spatially resolved measurements of the fine structures of the columnar vortices. Their results reveal that the asymptotic theory predicts accurately the velocity and vorticity profiles of the vortices in the flow regime of rotation-dominated convection, but deviate from the experimental results in weakly rotating convection. Three-dimensional experimental vorticity structure of vortices was measured by Fujita *et al.* (2020) through scanning velocity fields at different heights.

Numerical simulations in the full parameter space of rotating convection have revealed distinct flow structures with increasing buoyancy forcing, namely, cellular convection, convective Taylor columns, plumes, and geostrophic-turbulence (Julien *et al.* 2012; Stellmach *et al.* 2014; Nieves *et al.* 2014). It is shown that in the flow regime of CTC the shield structure of the columnar vortices weakens with increasing Ra and finally disappears. The violent vortex interactions then destroy the coherent columns and lead to the formation of plume-like structures (Stellmach *et al.* 2014). Rajaei *et al.* (2017) performed measurements of the spatial vorticity autocorrelations to reveal the periodicity of the flow structures. Their experimental results indicated a sharp change in the slope of the correlation function, indicating a transition from the cellular-columnar state to the plume state. Shi *et al.* (2020) measured the vorticity gradient at the shielding layer to determine quantitatively the strength of the vortex shield structures. They showed that the mean vorticity gradient followed two distinct scaling relations with increasing Ra , and suggested that a flow-state transition from weakly rotating convection to rotation-dominated, geostrophic convection.

Despite the large amount of studies devoted to explore the flow structures and spatial distribution of the vortices in rotating RBC, fewer efforts have been made to inspect the dynamics these vortices. Early experiment observations suggest that these convective vortices exhibit diverse dynamical states of horizontal motion, ranging from quasi-stationary, vortex merging to intensive advection (Bouznov & Golitsyn 1986; Zhong *et al.* 1993; Sakai 1997; Vorobieff & Ecke 2002; King & Aurnou 2012). Chong *et al.* (2020) demonstrate through both experiment and numerical simulation that the vortices undergo horizontally diffusive motion and resembles that of inertial Brownian particles, i.e., they move ballistically in short time but then diffusively in a large time scale. They reported that the diffusion motion of the vortices is in the type of pure Brownian motion, since the vortex velocity autocorrelation function decays exponentially in time, and the transition from ballistic to diffusive motion is sharp. Under rapid rotations the centrifugal force plays a role to influence the vortex motion. Noto *et al.* (2019) observed radial acceleration of the vortices that yielded a super-diffusive vortex motion in large time scale. Hu *et al.* (2021) used a convection cell placed

at a distance away from the rotation axis in which they can vary the Froude number with a fixed Ekman to study the centrifugal effects. They reported an onset of flow bifurcation above which the cold and hot vortices moved in opposite directions with cold (hot) vortices concentrated in the far (near) region. Ding *et al.* (2021) performed statistical analysis of the centrifugal motions of the convective vortices. They reported in the centrifugation-dominated flow regime the counterintuitive effect of hot vortices moving outward from the rotation axis, driven by long-range vortex interactions. Recently, Ding *et al.* (2022) reported that when periodic topographic structures are constructed on the heated boundary in rotating RBC, the stochastic translational motion of the columnar vortices can be strictly controlled to form stationary convection patterns with prescribed symmetries.

In this paper, we investigate the spatial distribution and dynamics of the convective vortices in rotating RBC. Our study covers the flow states from weakly rotating convection to rotation-dominated convection. The structure of the paper is organized as following. We introduce our experimental and numerical methods in § 2. Discussions of the vortex spatial distribution will be presented in § 3. We describe the random diffusion and centrifugal motion of single vortex in § 4, and provide an extended Langevin model to interpret the vortex dynamics. Inverse-centrifugal motion of cyclonic vortices are reported in § 5, where we give details of the different flow regimes for vortex motions. We discuss the dynamics of clustered vortices in the inverse-centrifugal flow regime in § 6. A summary and discussion of the results is provided in § 7.

2. Experimental and Numerical Methods

2.1. Experimental setup and parameters

The experimental apparatus was designed for high-resolution flow field measurements in rotating RBC. (Shi *et al.* 2020; Chong *et al.* 2020; Ding *et al.* 2021). Here we present only its essential features. The bottom plate of the convection cell was made of oxygen-free, high-conductivity copper (OFHC). Its bottom side was covered uniformly by parallel straight grooves. A main heater made of resistance wires was epoxied into the grooves. Seven thermistors were installed into the bottom plate, at a vertical distance of 3.5 mm from the top surface of the plate. The main heater was operated in a digital feedback loop in conjunction with these thermistors to hold the bottom-plate temperature as a constant with a stability of a few milli-Kelvin. For the purpose of flow visualization we used a top plate made by a 5 mm thick sapphire disc. A thermal bath that contained circulating coolant was constructed over the sapphire plate and regulated its temperature. During the experiment the temperature fluctuation of top plate was within 0.005 K.

The temperature difference between the bottom plate and the ambient air may induce thermal perturbations to the experiment. To eliminate mostly this temperature difference, a bottom adiabatic shield was installed under the bottom plate. This thermal shield was covered by a bottom-shield heater, with a thermistor located at the center of the shield. A second auxiliary heater was wound around the periphery of the shield and the local temperature there was measured by a second thermistor. Both heaters worked in conjunction with their relevant thermistors to maintain the bottom-shield temperature the same as the bottom-plate temperature.

In between the top- and bottom-plate was a cylindrical sidewall made of plexiglas in thickness of 3 mm. Thermal protection towards the sidewall was provided by a separate thermal side shield. It was a thin cylindrical ring made of aluminum, with a spiral aluminum tube wound on its outer surface. A circulating flow of coolant passed through the aluminum tube kept the side-shield temperature at the mean fluid temperature. Most of the spatial

volume in between the thermal shields and the convection cell was filled with low-density open-pore foam to prevent convective air flows. The aforementioned two coolant circuits were brought into the rotary table through a rotary union. It was a four-passage feed through equipped with a slip ring for electrical leads. The rotary table rotated clockwise driven by an electric servo-motor. All components of the convection cell were installed on the rotary table.

In the present study we used two cylindrical cells with an inner diameter $D_0=240$ mm, and fluid height $H=63.0$ (120.0) mm, yielding the aspect ratio $\Gamma_a=D_0/H=3.8$ (2.0). We report here mainly measurements in the cell with $\Gamma_a=3.8$ unless otherwise noted. Deionized water was the working fluid with a constant Prandtl number $Pr=\nu/\kappa=4.38$. The experiment was conducted in the range $2.0 \times 10^7 \leq Ra \leq 2.7 \times 10^8$ of the Rayleigh number $Ra=\alpha g \Delta T H^3 / \kappa \nu$ (α is the isobaric thermal expansion coefficient, g the acceleration of gravity, ΔT the applied temperature difference, κ the thermal diffusivity and ν the kinematic viscosity). All measurements were made at constant ΔT with Ω varying from 0 to 4.7 rad/s. The Ekman number $Ek=\nu/2\Omega H^2$ spanned $1.7 \times 10^{-5} \leq Ek \leq 2.7 \times 10^{-4}$. The Froude number $Fr=\Omega^2 D_0/2g$ was within $0 < Fr \leq 0.31$.

We conducted measurements of the horizontal velocity field (u_x, u_y) using a particle image velocimetry system installed on the rotary table. A thin light-sheet power by a solid-state laser illuminated the seed particles in a horizontal plane at a fluid height $z=H/4$. Images of the particle were captured through the top sapphire window by a high-resolution camera (2456×2058 pixels). Two-dimensional velocity fields were extracted by cross-correlating two consecutive particle images. Each velocity vector was calculated from an interrogation windows (32×32 pixels), with 50% overlap of neighboring sub-windows to ensure sufficient accuracy (Shi *et al.* 2020; Westerweel *et al.* 2013). Thus we obtained 154×129 velocity vectors on each frame, reaching a resolution of 2.0 mm for the velocity field. We identify the vortices through a two-dimensional Q-criterion. Considering the quantity $Q=(Tr\mathbf{A})^2-4det\mathbf{A}$ with the velocity gradient tensor $\mathbf{A}=[\partial(u_x, u_y)/\partial(x, y)]$, we define the vortex center as the minimum of Q within a vortex region satisfying $Q < -Q_{std}$. Here Q_{std} is the standard deviation of Q over the measured area $r \leq D_0/4$ (Chong *et al.* 2020; Ding *et al.* 2021). We adopt the method of vortex tracking introduced in (Ding *et al.* 2021) to obtain vortex trajectories.

2.2. Numerical method

In the direct numerical simulation (DNS) we solved the three-dimensional Navier-Stokes equations within the Boussinesq approximation:

$$\frac{D\vec{u}}{Dt} = -\nabla P + \left(\frac{Pr}{Ra}\right)^{1/2} \nabla^2 \vec{u} + \theta \hat{z} + \left(\frac{Pr}{RaEk^2}\right)^{1/2} \vec{u} \times \hat{z} - \frac{2rFr}{D} \theta \hat{r}, \quad (2.1)$$

$$\frac{D\theta}{Dt} = \frac{1}{(RaPr)^{1/2}} \nabla^2 \theta, \quad (2.2)$$

$$\nabla \cdot \vec{u} = 0. \quad (2.3)$$

Here \vec{u} is the fluid velocity, θ and P are the reduced temperature and pressure.

Equations (2.1)-(2.3) were nondimensionalized using H , ΔT and the free-fall velocity $U_f=\sqrt{\alpha g \Delta T H}$. The top (bottom) plate was isothermal with temperature $\theta_t=-0.5$ ($\theta_b=0.5$), and the sidewall was thermally insulated. As for the momentum boundary condition, all boundaries were non-slip. These equations were solved using the multiple-resolution version of *CUPS* (Kaczorowski & Xia 2013; Chong *et al.* 2018), which was a fully parallelized direct numerical simulation code based on finite volume method with 4th order precision. To improve computational efficiency without any sacrifice in precision, we used a multiple-

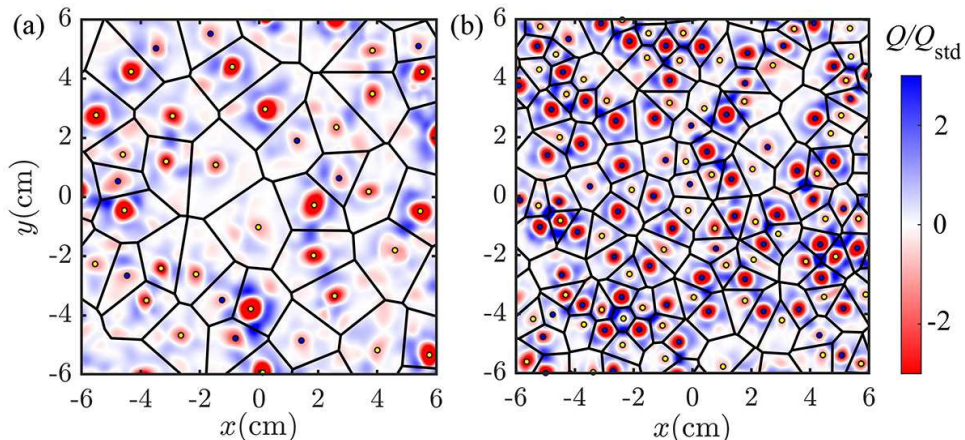


Figure 1: Spatial distribution of the vortices for weakly rotating convection (a) and rotation-dominated convection (b). The solid-line network constitutes the Voronoi diagram of the vortex centers. The background coloration represents distribution of the quantity Q/Q_{std} , with black (yellow) dots denoting the centers of anticyclones (cyclones). Results for $Ra=3.0\times 10^7$ and for $Ra/Ra_c=8.90$ (a) and $Ra/Ra_c=2.67$ (b).

resolution strategy, i.e., the momentum equation was solved in a coarser grid than the temperature one, allowing for a sufficient resolution to resolve the Batchelor and Kolmogorov length scales. The simulations were performed in a cylindrical domain with $\Gamma_a=4$, $Ra=2.0\times 10^7$, $Pr=\nu/\kappa=4.38$ and $1.3\leq Ra/Ra_c\leq 55$.

3. Vortex Spatial Distribution

In the rotating RBC, the spatial distribution and organization of the convective vortices depend sensitively on the strength of rotation and buoyancy. To demonstrate the distribution distribution of the columnar vortices, we present in figure 1 Voronoi diagrams of the vortex centers for two reduced Rayleigh numbers, $Ra/Ra_c=8.90$ and 2.67 , respectively. The background color of these diagrams represents distribution of the Q field, where vortices are shown in reddish color and the bluish areas in-between indicate regions of high flow strain. We see that under weak rotations the vortices appears randomly located with a broad size distribution for $Ra/Ra_c=8.90$. The Voronoi cells becomes smaller in average but with an even size-distribution for rapid rotations ($Ra/Ra_c=2.67$).

We calculate the probability density functions (PDFs) of Voronoi cell area normalized by the mean value $A/\langle A \rangle$. It has been shown that for randomly distributed entities in d -dimension space ($d\leq 3$), the PDF of the scaled areas (volumes) of the Voronoi cells is a standard Γ -distribution with the dimension d as the only fitting parameter:

$$P(x) = \frac{[(3d+1)/2]^{(3d+1)/2}}{\Gamma[(3d+1)/2]} x^{\frac{3d-1}{2}} e^{-[(3d+1)/2]x} \quad (3.1)$$

Here the denominator is a Γ function. For two-dimensional distributions we have $P_2(x)=7^{7/2}2^{-7/2}x^{5/2}e^{-7x/2}/\Gamma(7/2)$. Figure 2a shows that for a sufficiently large Ra/Ra_c , $P(A/\langle A \rangle)$ follows closely the standard Γ -distribution $P_2(x)$. With the increasing rotation rate (decreasing Ra/Ra_c), the PDFs of the Voronoi cell area show different behavior from that of the standard Γ -distribution. We see that the PDFs have a smaller possibility for very large and small cells than for random distributed one, whereas a larger probability

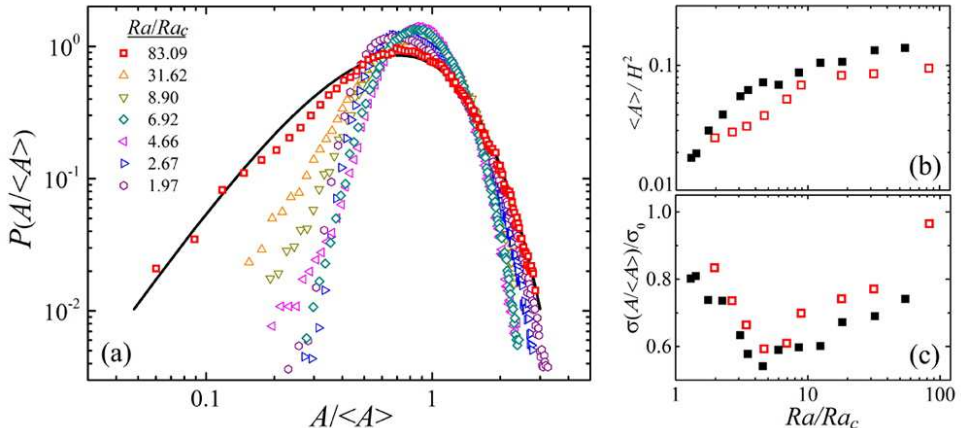


Figure 2: (a) PDFs of the Voronoi cell area $P(A/\langle A \rangle)$ for various Ra/Ra_c . The solid curve represents the two-dimensional Γ -distribution $P_2(A/\langle A \rangle)$. (b) The normalized mean area $\langle A \rangle / H^2$ of the Voronoi cells as a function of Ra/Ra_c . (c) The rescaled standard deviation $\sigma(A/\langle A \rangle) / \sigma_0$ as a function of Ra/Ra_c , with $\sigma_0 = \sqrt{2/(3d+1)} = \sqrt{2/7}$. Open symbols: experimental data for $Ra = 3.0 \times 10^7$. Closed symbols: numerical data for $Ra = 2.0 \times 10^7$.

for $A/\langle A \rangle \approx 1$. These results suggest that the vortices are indeed randomly distributed for $Ra/Ra_c = 83.09$ and have a trend of forming regular vortex lattice when Ra/Ra_c decreases.

Figures 2b and 2c present the mean value $\langle A \rangle$ and the variance $\sigma(A/\langle A \rangle)$ of the Voronoi cell area as functions of Ra/Ra_c . Both our experimental and numerical data show that $\langle A \rangle$ decreases monotonically with decreasing Ra/Ra_c , signifying an increasing vortex number density. The variance $\sigma(A/\langle A \rangle)$, however, exhibits the interesting trend that it first decreases till reaching a minimum value at $Ra/Ra_c \approx 5$. When $Ra/Ra_c \leq 5$, $\sigma(A/\langle A \rangle)$ starts to increase. The emergence of the minimum of $\sigma(A/\langle A \rangle)$ at $Ra/Ra_c \approx 5$ can be seen also in figure 2a. The decreasing of $\sigma(A/\langle A \rangle)$ for $Ra/Ra_c \geq 5$ implies the homogenized size-distribution of the Voronoi cells with decreasing Ra/Ra_c . For $Ra/Ra_c \leq 5$, however, the increase of $\sigma(A/\langle A \rangle)$ is ascribed to the rapid decreasing of $\langle A \rangle$ with decreasing Ra/Ra_c as shown in figure 2b.

4. Single Vortex Dynamics

We discuss in this section the rich dynamics of translational motion of sparsely distributed vortices observed in a horizontal plane, including Brownian-type random diffusion in the flow regime of weakly rotating convection, and centrifugal motion with stochastic fluctuations in the centrifugation-influenced convection regime. Some of our results have been reported briefly before (Chong *et al.* 2020; Ding *et al.* 2021). Here we present a full description and provide more comprehensive discussions of these two types of stochastic vortex motion.

4.1. Randomly diffusive motion of vortices in weakly rotating convection

Through tracking the horizontal motion of the vortices, we obtain their trajectories $\vec{r}(t)$ of the vortices, and calculate the mean-square-displacement (MSD) for the vortices for a given time interval t , i.e., $\langle \delta r^2 \rangle(t) = \langle (\vec{r}(t) - \vec{r}(0))^2 \rangle$. Figure 3 shows $\langle \delta r^2 \rangle / t$ as a function of t for several Ra/Ra_c in the full parameter range. We first discuss here results in weakly rotating convection, where the centrifugal effect is minor. It is clearly see that in this flow state the vortex motion undergoes a transition from the ballistic regime where $\langle \delta r^2 \rangle$ increases as t^2 in short time, to a diffusive regime where $\langle \delta r^2 \rangle$ increases linearly and $\langle \delta r^2 \rangle / t$ approaches

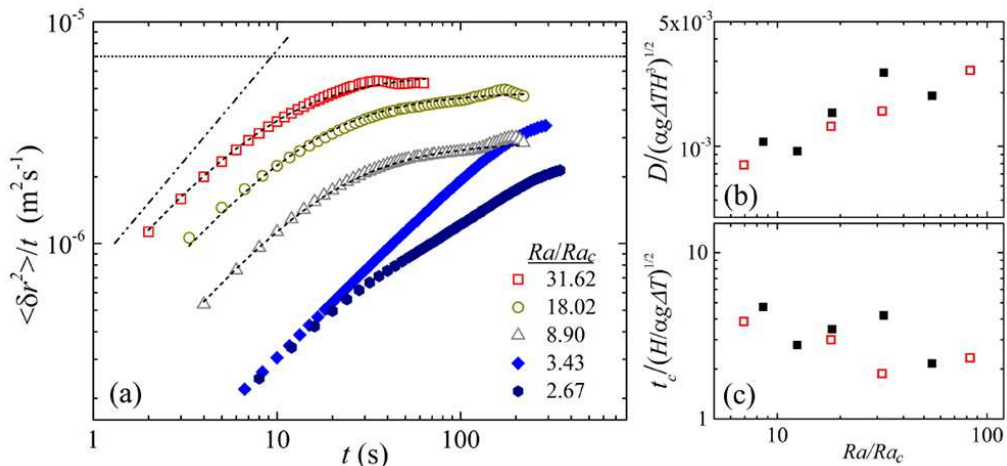


Figure 3: (a) Results of $\langle \delta r^2 \rangle / t$ as a function of t for various Ra/Ra_c . The dashed lines present the theoretical fits to the data for weakly rotating convection based on (4.2). The dash-dot line indicates a scaling $\langle \delta r^2 \rangle \sim t^2$ in the ballistic regime. Results for $Ra = 3.0 \times 10^7$. (b) and (c) show the normalized diffusivity D and transitional time t_c as a function of Ra/Ra_c . Open symbols: experimental data for $Ra = 3.0 \times 10^7$. Closed symbols: numerical data for $Ra = 2.0 \times 10^7$.

a constant in long time. Thus the vortex motion resembles the random motion of Brownian particles, which can be described by the Langevin Equation:

$$\ddot{r} + \dot{r}/t_c = \xi(t), \quad (4.1)$$

where the two momentum terms on the left-hand-side are the inertia and the viscous force, respectively. $\xi(t)$ represents the stochastic force acting on the vortices that is modeled as $\langle \xi(t) \rangle = 0$ and $\langle \xi(t) \xi(t + \Delta t) \rangle = q \delta(\Delta t)$. Here q represents the strength of the stochastic force and $\delta(t)$ is a Dirac function. Solving Eq. 4.1 one obtains the solution for the MSD of the vortices:

$$\langle \delta r^2 \rangle = 2Dt [1 - t_c/t(1 - e^{-t/t_c})]. \quad (4.2)$$

Here t_c is the transitional time from the ballistic to diffusive regime. It represents the characteristic time scale of relaxation for the diffusive vortex motion. D is the diffusivity that relates to the noise strength through $D = qt_c^2$ according to the fluctuation-dissipation theorem. The dashed lines in figure 3a are fitting curves $\langle \delta r^2 \rangle / t$ to the experimental data according to (4.2), with two fitting parameters (t_c, D) that depends on Ra/Ra_c . Figures 3b and 3c present results of t_c and D as functions of Ra/Ra_c . Both our experimental and numerical data show that with decreasing Ra/Ra_c , t_c increases while D decreases monotonically. The increasing relaxation time t_c when Ra/Ra_c decreases is not yet well understood, but we infer that in the flow regime of weakly rotating convection the vertical scale of the vortices grows when the rotating rate Ω increases since the vortex structure has not fully developed to penetrate the whole fluid layer (Shi *et al.* 2020). The larger vertical scale of the vortices results in a greater inertia of motion and thus an increasing relaxation time t_c for the translational vortex motion. The apparent decreasing in D signifies the reducing intensity of the stochastic force acting on the vortices when Ra/Ra_c decreases.

To gain deep insight into the statistical properties of the vortex motion in the state of weakly rotating convection, we study the PDFs of the vortex displacement $P(dx, dt)$ in one dimension dx for different time intervals dt . Figures 4a and 4b show experimental and

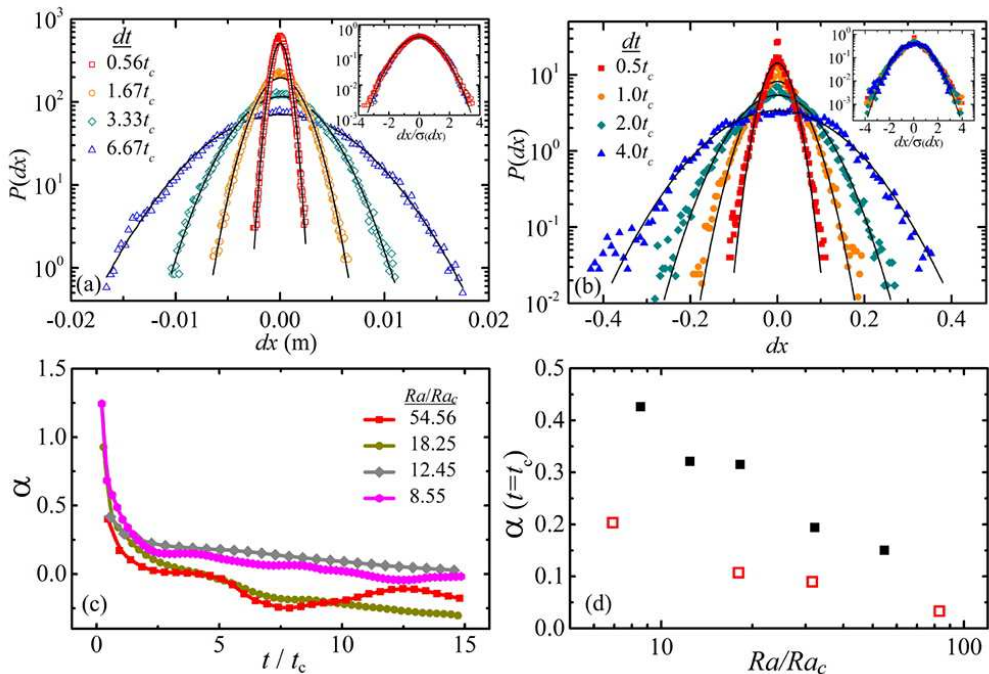


Figure 4: (a) and (b) PDFs of the vortex displacement $P(dx)$ at various time intervals dt . Experimental (a) and numerical (b) data for $Ra/Ra_c=18.0$. Insets in (a) and (b) show the rescaled PDFs $P(dx/\sigma(dx))$ where the vortex displacement dx is normalized by its standard deviation $\sigma(dx)$. (c) The non-Gaussian parameter α as a function of t/t_c . (d) α as a function of Ra/Ra_c for $t = t_c$. Open symbols: experimental data for $Ra=3.0 \times 10^7$. Closed symbols: numerical data for $Ra=2.0 \times 10^7$.

numerical data for $Ra/Ra_c=18.0$, respectively. We see that for a large time interval $dt \geq t_c$, $P(dx)$ is Gaussian to good precision, as one would expect for normal Brownian motion. For very small time interval $dt \leq t_c$, however, $P(dx)$ appears to deviate from a Gaussian function. In order to investigate the deviation of $P(dx)$ from Gaussian distribution with decreasing dt , we calculate the excess kurtosis α , which characterizes the departure from Gaussianity, $\alpha = \langle (dx - \langle dx \rangle)^4 \rangle / [3 \langle (dx - \langle dx \rangle)^2 \rangle^2] - 1$. Thus $\alpha=0$ indicates a perfect Gaussian distribution and a large α signifies a departure from Gaussian. Figure. 4c shows results of α as a function of dt/t_c for two sets of Ra/Ra_c . One sees that $\alpha \leq 0.1$ for large time interval $dt \geq t_c$. However, when dt decreases below t_c α increases rapidly and becomes significant for very small dt . Results of the MSD and the PDFs of the vortex displacement (figures 3 and 4) suggests that the at very short time scales the vortex motion undergoes non-Gaussian yet Brownian diffusion. A full theoretical interpretation of the diffusive dynamics of the vortices remains yet to be studied.

Here we infer that in a small time scale the random motion of the vortices, driven by the turbulent fluctuations of the background flows, is largely disturbed by the passing vortices. The vortex interactions, such as merging (annihilation) of same(opposite)-sign neighboring vortices, results in intermittent but deterministic horizontal movements of the vortices in short time. The observed PDFs of the vortex displacement in this time scale is thus non-Gaussian. As the time interval dt increases and so does the vortex displacement dx , the intermittent perturbation from single adjacent vortex gives way to the complex interactions from multiple neighboring vortices that appear to have stochastic spatiotemporal properties.

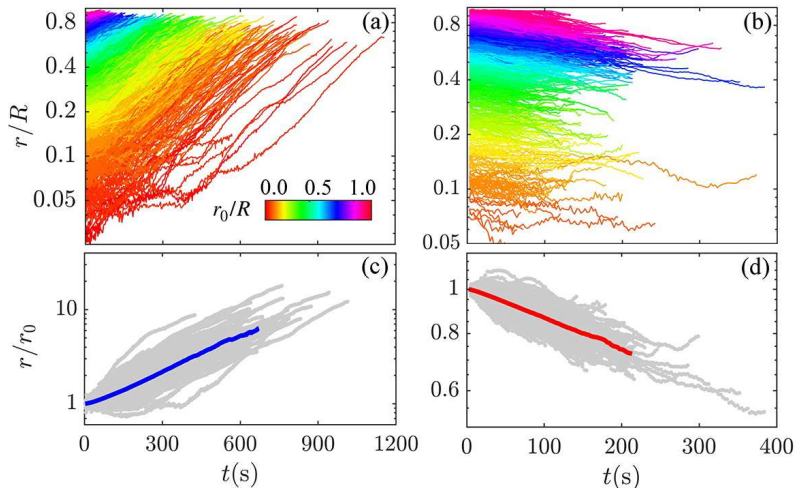


Figure 5: Space-time plots of representative radial trajectories of the vortices. (a) and (b) show data of $r(t)/R$ for anticyclones and cyclones, respectively. The color represents the initial radial position r_0/R of the vortices. (c) and (d) show $r(t)/r_0$ for anticyclones and cyclones. The blue line in (c) and the red line in (d) represent the ensemble-averaged trajectories $\langle r/r_0 \rangle_{\xi}(t)$. In (b) and (d), data for cyclones that exhibit inward motions are shown to illustrate normal centrifugal effects. Data are for $Ra=3.0 \times 10^7$, $Ra/Ra_c=1.97$ and $Fr=0.27$.

In addition, owing to the large-amplitude background turbulent fluctuations that dominate the vortex motion in large time scales, the PDF of the vortex displacements return to Gaussianity. In figure 4d we investigate the non-Gaussian parameter α as a function of Ra/Ra_c for a given time interval $dt=t_c$. Both our experimental and numerical data suggest that in this weakly rotating regime α increases when Ra/Ra_c decreases. A similar trend of increasing α with decreasing Ra/Ra_c is found when other time intervals dt are chosen.

4.2. Stochastic motion of vortices driven by centrifugal force

Figure 3a shows that in the state of rapidly rotating convection the MSD $\langle \delta r^2 \rangle(t)$ of the vortices increases faster than a linear function of t for large time, which implies super-diffusive behavior of the vortices in rapidly rotating convection. This phenomenon is attributed to the centrifugal effect (See. e.g. Noto *et al.* (2019); Hu *et al.* (2021, 2022)): in a reference frame of rotation warm (cold) vortices are driven radially inwards (outwards) by the centrifugal force. Such radial motions add to the displacement of the vortices and result in their superdiffusion in large time. In the parameter range considered in our study, such a centrifugal effect acts as an external forcing that is capable to alter the horizontal motion of the vortices, but not as strong to modify their coherent flow structures (Horn & Aurnou 2018, 2019).

Figures 5a and 5b are space-time plots of representative radial trajectories of anticyclones and cyclone, respectively. The radial positions of the vortices are shown as functions of time for various initial positions r_0 . It appears that the radial displacements $r(t)$ of anticyclones (cyclones) increase (decrease) approximately exponentially in time. Figures 5c and 5d present the scaled radial trajectories of the vortices $r(t)/r_0$, corresponding to the same data sets in figures 5a and 5b, respectively. We then compute the ensemble-averaged scaled radial trajectories $\langle r/r_0 \rangle_{\xi}$, which is the average of $r(t)/r_0$ of all trajectories for a given time t . Results of $\langle r/r_0 \rangle_{\xi}(t)$ are shown by the thick blue (red) lines for anticyclones (cyclones), which indicate clearly the exponential growth (decay) of the vortex radial displacements.

In order to understand the super-diffusive behavior of the vortices in a background of stochastic movements, we propose a model to describe the radial vortex motion under the centrifugal force. Our model has been introduced before (Ding *et al.* 2021). For the purpose of integrity for the present work, we provide here brief discussions of its derivation and predictions. We consider Langevin-type equations of motion for the vortices, i.e., $m\ddot{r} + \eta\dot{r} \pm m\alpha\delta T\Omega^2 r = \xi^*(t)$. The vortices are subject to the centrifugal force expressed in terms of $\pm m\alpha\delta T\Omega^2 r$ for warm cyclones (plus sign) and cold anticyclones (minus sign). Here m is inertia mass of the vortices and δT is the temperature difference between the vortex and the background fluid. We define the relaxation time $t_c = m/\eta$ and the centrifugal coefficient $\zeta = \alpha\delta T\Omega^2$ to obtain:

$$\ddot{r} + \dot{r}/t_c \pm \zeta r = \xi(t) \quad (4.3)$$

Here $\xi = \xi^*(t)/m$ is the rescaled strength of background turbulent fluctuation, which modeled by a δ -correlated white noise $\langle \xi(t)\xi(t+\Delta t) \rangle = \delta(\Delta t)D/t_c^2$. D is the diffusivity. Defining valuables $\lambda_{1,2} = \pm \sqrt{-\zeta + 1/(4t_c^2)} + 1/(2t_c)$ for cyclones and $\lambda_{1,2} = \pm \sqrt{\zeta + 1/(4t_c^2)} + 1/(2t_c)$ for anticyclones, one derives from (4.3) the solution for the first moment of radial displacement:

$$\langle r/r_0 \rangle_\xi = \frac{\lambda_1}{\lambda_1 - \lambda_2} e^{-\lambda_2 t} - \frac{\lambda_2}{\lambda_1 - \lambda_2} e^{-\lambda_1 t} \quad (4.4)$$

where $\langle \dots \rangle_\xi$ presents average over all trajectories of the vortices. In the large-time limit ($t \gg t_c$) the first moment of radial displacement asymptotes to a single exponential function, $\langle r/r_0 \rangle_\xi \approx \lambda_1 e^{\pm \lambda^* t} / (\lambda_1 - \lambda_2)$. Here $\lambda^* = |1/(2t_c) - \sqrt{1/(4t_c^2) \pm \zeta}|$ is the fastest growth (or slowest decay) rate for anticyclones (cyclones), which represents the mobility of vortices in the context of centrifugal acceleration. One thus derive the asymptotic solution of the ensemble-averaged velocity in large time,

$$\langle u_r/r_0 \rangle_\xi \approx \frac{\lambda_1 \lambda^* t}{\lambda_1 - \lambda_2} e^{\pm \lambda^* t} \approx \lambda^* \langle r/r_0 \rangle_\xi \quad (4.5)$$

where u_r is the radial velocity of vortices.

We can further obtain the second moment of the radial displacement as follows:

$$\langle [r(t) - \langle r(t) \rangle_\xi]^2 \rangle_\xi = \frac{D}{t_c^2 (\lambda_2 - \lambda_1)^2} \left[\frac{1 - e^{-2\lambda_1 t}}{2\lambda_1} + \frac{1 - e^{-2\lambda_2 t}}{2\lambda_2} - \frac{2 - 2e^{-(\lambda_1 + \lambda_2)t}}{\lambda_1 + \lambda_2} \right] \quad (4.6)$$

The first moment $\langle r/r_0 \rangle_\xi$ represents the mean radial displacement of the vortices, while the second moment $\langle [r(t) - \langle r(t) \rangle_\xi]^2 \rangle_\xi$ measures the standard deviation of the radial vortex displacements from the mean (see figures 5c and 5d for demonstrations). As reported elsewhere (Ding *et al.* 2021), our theoretical predictions (4.4) and (4.6) of these statistical quantities are in close agreements with the experimental data. Our model provides satisfactorily explanations of the super-diffusive behavior of the convective vortices observed in rotating RBC systems (e.g. Noto *et al.* (2019); Ding *et al.* (2021)).

5. Anomalous Regime of Vortex Motion

The centrifugal force gives rise to the radial vortex motion, resulting in radial-dependence of the vorticity field. Figure 6 shows as functions of the radial position, the mean values of the radial velocity $\langle u_r \rangle_\xi$, number density $\langle n \rangle_\xi$ and vorticity magnitude $\langle |\omega| \rangle_\xi$ of both types of vortices. Four distinct flow regimes are clearly identified. We first find in a weakly rotating regime ($Ra/Ra_c = 54.8$ and $Fr = 0.030$) that $\langle u_r \rangle_\xi$ for both types of vortices fluctuates around zero, indicating the absence of radial motion (figure 6a). In this flow regime, we note that

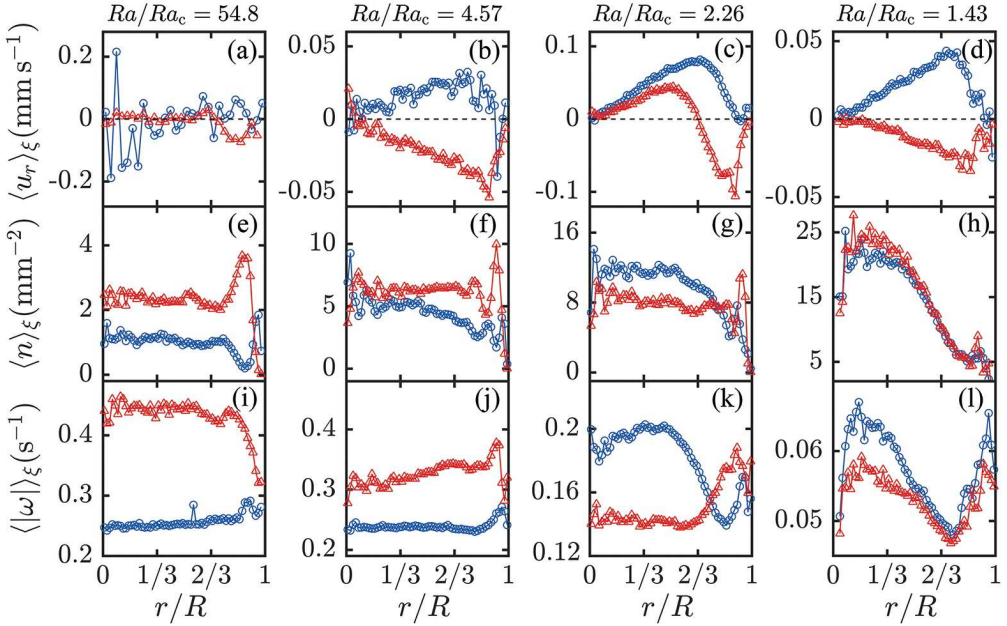


Figure 6: The ensemble-averaged radial velocity $\langle u_r \rangle_\xi$ (a-d), vortex density $\langle n \rangle_\xi$ (e-h) and vorticity amplitude $\langle |\omega| \rangle_\xi$ (i-l) as functions of r/R . $\langle \cdot \rangle_\xi$ denotes the ensemble average. Results are for $Ra=2.0 \times 10^7$ with $Ra/Ra_c=54.8$ and $Fr=0.030$ (a,e,i), $Ra/Ra_c=4.57$ and $Fr=0.044$ (b,f,j), $Ra/Ra_c=2.26$ and $Fr=0.12$ (c,g,k), $Ra/Ra_c=1.43$ and $Fr=0.24$ (d,h,l), respectively. Red triangles (blue circles) denote cyclonic (anticyclonic) data.

the mean values of number density $\langle n \rangle_\xi$ and vorticity magnitude $\langle |\omega| \rangle_\xi$ for cyclones are significantly greater than those for anticyclones (figures 6e and 6i). This is the case because anticyclones are down-welling vortices generated from the top boundary. When observed at the lower half of the fluid layer, they travel a longer distance to the measured fluid height ($z=H/4$) than the upwelling vortices (cyclones), and their momentum and vorticity have been largely dissipated by the background turbulence. $\langle n \rangle_\xi$ and $\langle |\omega| \rangle_\xi$ for the two types of vortices would be equal if measured at $z=H/2$ (see discussions in reference (Ding *et al.* 2021)). In the sidewall-region ($r/R > 0.85$) large fluctuations of all the measured variables appear owing to the intensive perturbation of the flow field by the boundary zonal flows (Zhang *et al.* 2020; de Wit *et al.* 2020).

When the rotating rate increases ($Ra/Ra_c=4.57$, $Fr=0.044$), we see that $\langle u_r \rangle_\xi$ of anticyclones (cyclones) is larger (smaller) than zero indicating that anticyclones (cyclones) move away from (towards) the rotation axis under the centrifugal force. Figure 6b shows that $\langle u_r \rangle_\xi$ increases (or decreases) linearly with r for anticyclones (cyclones), which is well predicted by our model (4.5). Cyclonic vortices still possess a greater number density and vorticity magnitude than those of anticyclones at the measurement height (figures 6f and 6j). With further increase of Ω the centrifugal effect becomes dominant. For $Ra/Ra_c=2.26$, $Fr=0.12$, we note that unexpectedly $\langle u_r \rangle_\xi$ of both vortices are positive and increase linearly with r in the inner region (figure 6c), signifying that cyclones exhibit outward motion that is opposite to the centrifugal effect. For both types of vortices $\langle u_r \rangle_\xi$ reaches a maximum at a radial position that depends on Ra/Ra_c , and then decreases with larger r in the outer region. We find in the central region both the number density and vorticity magnitude of anticyclones exceed those of the cyclones (figures 6g and 6k). In the limit of rapid rotation

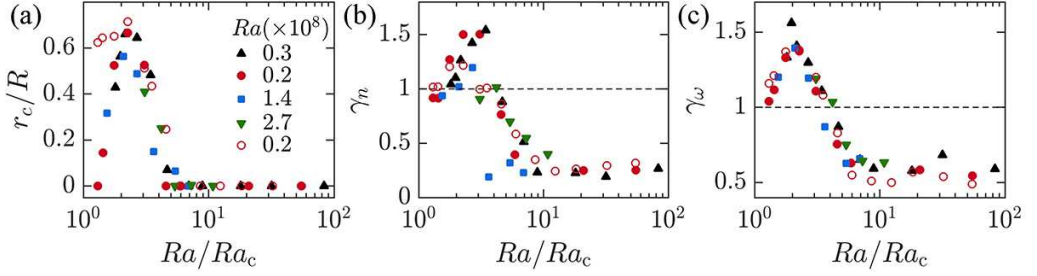


Figure 7: (a) The outer region boundary r_c/R for the inverse centrifugal motion of cyclones. (b) The ratio γ_n of the number density of anticyclones over cyclones. (c) The ratio γ_ω of vorticity amplitude of anticyclones over cyclones. Results are shown as functions of Ra/Ra_c . Data for $Ra=2.0 \times 10^7$ and $\Gamma_a=3.8$ (circles), $Ra=3.0 \times 10^7$ and $\Gamma_a=3.8$ (up-triangles), $Ra=1.4 \times 10^8$ and $\Gamma_a=2.0$ (squares), $Ra=2.7 \times 10^8$ and $\Gamma_a=2.0$ (down-triangles). The open circles are numerical data.

with $Ra/Ra_c=1.43$, $Fr=0.24$, the cyclones are found to take up the inward radial motion with $\langle u_r \rangle_\xi$ decreases linearly with r in the inner region (figure 6d). The profiles of $\langle n \rangle_\xi(r)$ and $\langle |\omega| \rangle_\xi(r)$ for both types of vortices show similar radial-dependence, suggesting that the symmetry of the vorticity field restores near the onset of convection.

We further investigate the parameter regime in which the inverse centrifugal motion of cyclones occurs. We define the region boundary r_c for anomalous vortex motion as follows: the mean radial velocity of cyclones $\langle u_r \rangle_\xi \geq 0$ for $r \leq r_c$, and $\langle u_r \rangle_\xi < 0$ for $r > r_c$. As shown in figure 6c, r_c is thus the second zero crossing of the radial profile $\langle u_r \rangle_\xi(r)$. Figure 7a shows r_c/R as a function of Ra/Ra_c . We find $r_c=0$ for $Ra/Ra_c \geq 4$. r_c exceeds zero when Ra/Ra_c decreases below 4, reaching a peak at $Ra/Ra_c \approx 2$. With further decreasing in Ra/Ra_c we see that r_c decreases, and the experimental data indicate the trend that r_c eventually approaches to zero near the onset of convection $Ra/Ra_c \approx 1$. Near onset our numerical data show a higher value of r_c than the experimental one, presumably owing to the insufficient numerical data evaluating the velocity profile $\langle u_r \rangle_\xi(r)$. Otherwise results of r_c/R for various Ra collapse approximately onto one single curve. We calculate in the central region ($r \leq 0.5R$) the ratios of the number density γ_n and the vorticity magnitude γ_ω of the anticyclones over the cyclones. Figures 7b and 7c present results of γ_n and γ_ω as functions of Ra/Ra_c , respectively. We see that data of γ_n and γ_ω for various Ra also exhibit similar dependence of Ra/Ra_c . For $Ra/Ra_c > 4$, γ_n and γ_ω are constants irrespective of Ra/Ra_c . γ_n and γ_ω increase when $Ra/Ra_c \leq 4$ and have a maximum at $Ra/Ra_c \approx 2$. When $Ra/Ra_c < 2$ the two ratios γ_n and γ_ω decrease with further decreasing Ra/Ra_c and approaches unity at the onset of convection.

The observed asymmetry of the vorticity field in the anomalous regime is attributed to the centrifugal effect. As the centrifugal force drives continuously hot (cold) fluid parcels towards (away from) the center of the convection cell, the background fluid temperature in the central region increases and exceeds global mean fluid temperature (Hart & Olsen 1999; Liu & Ecke 2011; Horn & Aurnou 2019). Thus in the central region, the temperature difference of the cold anticyclones from the background fluid becomes greater than that of the warm cyclones. Since such a temperature anomaly is proportional to the buoyancy forcing on the vortices, it is positively correlated to the vorticity magnitude of the vortices (Portegies *et al.* 2008; Grooms *et al.* 2010). It is also believed that the fluid warming in the central region enhances the stability of the anticyclonic flows, leading to a larger population of anticyclones. As a results, we find in figures 7b and 7c that both the number density and the vorticity magnitude of the anticyclones exceeds the cyclonic ones.

The aforementioned vortex dynamics and symmetric properties of the vorticity field reveal four distinct flow regimes depending on the rotation rates: (I) A randomly diffusive regime in the slow rotating limit with Ra being one order in magnitude larger than Ra_c . In this flow regime the vortices move in a random manner, yielding $\langle u_r \rangle_\xi \approx 0$, and r_c/R is close to zero. Since in the measured fluid height the cyclones have a greater population as well as a larger vorticity magnitude than the anticyclones, γ_n and γ_ω are both less than unity but independent of Ra/Ra_c . (II) A centrifugation-influenced regime ($4 \leq Ra/Ra_c \leq 10$) where the magnitude of $\langle u_r \rangle_\xi$ increases linearly with r (figure 6b). We observe that warm cyclones (cold anticyclones) move radially inward (outward), which is in agreement with the centrifugal effect. (III) An Inverse-centrifugal regime ($1.6 \leq Ra/Ra_c \leq 4$) in which the cyclones exhibits anomalous outward motion in the inner region with $r \leq r_c$ (figure 6c). In this flow regime anticyclones become the dominant flow structures in the sense that both γ_n and γ_ω exceed far above unity (figures 7b and 7c). In the outer region ($r \geq r_c$) the centrifugal effect of fluid warming becomes insignificant, we observe there inward cyclonic motion, as $\langle u_r \rangle_\xi$ for cyclones decreases with increasing r and becomes negative. (IV) The asymptotic regime in the rapid rotation limit ($Ra/Ra_c < 1.6$) where r_c approaches zero and the opposite radial motions of cyclones and anticyclones recover (figure 6h).

6. Vortex Cluster Dynamics

6.1. Formation of Vortex Clusters

We have seen that in the inverse-centrifugal regime the symmetry of vorticity field is broken with the anticyclonic vortices dominating the cyclones both in strength and population. We show below that in this regime the vortices self-organize into clusters in which the anticyclones dominate the long-range correlated vortex motion, leading to the inverse centrifugal motion of the cyclones.

Figure 8a presents an example of instantaneous spatial distribution and motion of the vortices in the inverse-centrifugal regime. We find that the adjacent vortices often move in similar directions and aggregate locally, forming vortex clusters. Here we adopt the following two criteria to identify vortex clusters (See e.g. Chen *et al.* (2012)):

- 1) The distance of two neighboring vortices is smaller than 1.5 times the mean vortex diameter;
- 2) The angle between the velocity of two adjacent vortices is less than θ^* .

Our analysis over the range $30^\circ \leq \theta^* \leq 75^\circ$ confirms that the results of correlated vortex motion are not sensitive to the choice of θ^* . In the following we discuss statistical properties using $\theta^* = 60^\circ$.

In figure 8 vortex clusters are identified using the aforementioned criteria. In this Voronoi diagrams of vortex centers, each cluster is enclosed by thick lines, with Voronoi cells within the same cluster printed in the same color. We define the cluster length L as the largest distance between two vortex centers within the cluster, and compute the number of vortices N with each cluster. Figure 8b shows L as a function of N for $Ra = 3 \times 10^7$ and $Ra/Ra_c = 1.97$. We find that $L(N)$ can be well fitted by a power function, $L = A_c N^{\beta_c}$. Assuming that the distance between two adjacent vortices d_{vv} is independent of N , the power exponent β_c then reveals the dimensional properties of clusters. When $\beta_c = 0.5$ vortices in a cluster are distributed isotropically in a two-dimensional plane. When $\beta_c = 1$, vortices line up to form one-dimensional clusters. Figure 8c shows that within the full parameter range of Ra/Ra_c studied, β_c increases slightly from 0.80 to 0.87 with increasing Ra/Ra_c , suggesting a fractal property of the vortex clusters: vortices in a cluster have a weak preference to be arranged

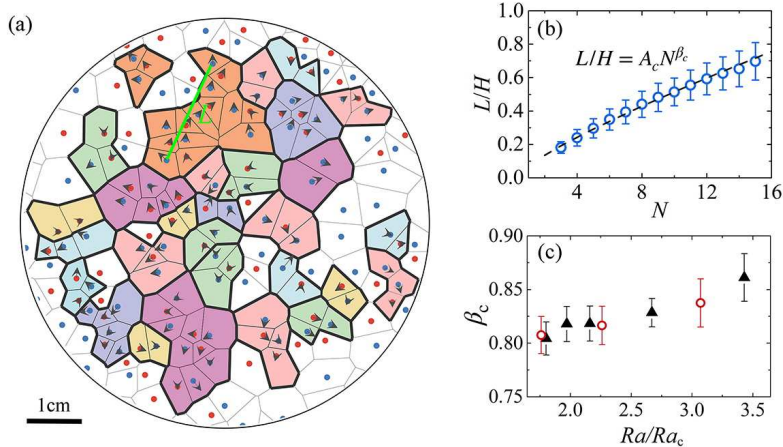


Figure 8: (a) Spatial distribution of vortex clusters. The polygons represent the Voronoi tessellations of the vortex centers. Voronoi cells within the same vortex cluster are printed in the same color and enclosed by thick lines. The blue (red) dots denote the centroid of anticyclonic (cyclonic) vortices with arrows indicating their velocity direction. Experimental data in a region of $r \leq 0.7R$ are shown. (b) The normalized cluster length L/H as a function of cluster size N . The dashed line represents the fitted power function $L/H = A_c N^{\beta_c}$, where $A_c = 0.079$ and $\beta_c = 0.81$. Data in (a) and (b) are for $Ra = 3.0 \times 10^7$ and $Ra/Ra_c = 1.97$. (c) The exponent β_c as a function of Ra/Ra_c for various Ra numbers. Open circles: $Ra = 2.0 \times 10^7$. Solid triangles: $Ra = 3.0 \times 10^7$.

along one direction, while the horizontal span of the cluster is not isotropic but dependent on the orientation.

Within each cluster the vortices exhibit long-range correlated motions. We attribute these correlated vortex motions to the vortex-vortex interaction that occurs in a convection state where the vortices are densely distributed. Figure 9a shows the PDF $p(l/r_a)$ of the distance l between an downwelling vortex (anticyclone when observed in the lower half fluid layer) and its neighboring upwelling vortices for various Ra/Ra_c . Here r_a is the radius of the downwelling vortex. One sees that $p(l)$ has an apparent maximum at $l_m = cr_a = 1.593r_a$. Here the constant c is the ratio of first minimum over the first zero of the zero-order Bessel function J_0 . Since $p(l)$ represents the probability finding upwelling vortices at a distance l from a downwelling vortex, it reflects the interactions between adjacent counter-rotating vortices. Figure 9b shows an example of the vorticity profile $\omega(s)$ of two opposite-sign, neighboring vortices, with the coordinate s measuring the distance to the center of the downwelling vortex along the connecting line. We see that within the core region ($s < l_m$) the vorticity profile $\omega(s)$ is well described by $J_0(s)$. $\omega(s)$ reaches a first minimum at $s = l_m$ where $p(l)$ is maximum. Such a pair-wise vorticity profile is commonly observed within vortex clusters in our experiment.

We provide the following interpretation for the most probable vortex separation l_m . We consider the motion of warm, upwelling vortices in the vicinity of a cold, downwelling vortex. Observed in the lower half fluid layer ($z < H/2$), the cold vortex gives rise to negative background vorticity gradient in the core region ($s < l_m$), but a positive vorticity gradient outside the vortex core ($s > l_m$) (see a schematic drawing in figure 9c). The theory of vortex motion on a vorticity gradient (Schecter & Dubin 1999) suggests that a upwelling vortex, which possesses negative vorticity in the lower half layer in our case, moves down the vorticity gradient due to the background shear flow. Thus, inside the core region ($s < l_m$) the upwelling vortex moves away from the downwelling vortex center, but moves towards it

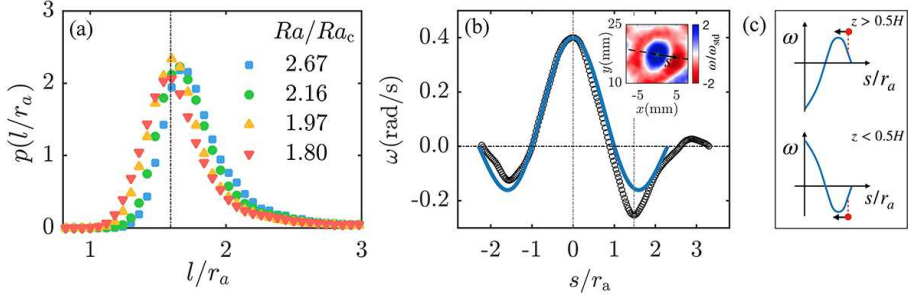


Figure 9: (a) PDFs of the distance l between an anticyclone and its neighboring cyclones within a cluster, normalized by the radius of the anticyclone r_a . The vertical dashed line shows a maximum of $p(l/r_a)$ at $l=l_m=cr_a$. (b) Vorticity profile $\omega(s/r_a)$ of an opposite-sign vortex pair along the centerline s . The anticyclonic radius r_a is defined by the radial position where $\omega(s/r_a)$ crosses zero. Open circles: experimental data. Solid line: the scaled zero-order Bessel functions: $J_0(k_s/r_a)\omega(0)/J_0(0)$, where $k=2.405$ is the first zero of J_0 . The two vertical dashed lines indicate the centers of the anticyclone and the cyclone at $s_1=0$ and $s_2=cr_a$. The inset shows the vorticity distribution of this vortex pair with the dashed line being the centerline. (c) Schematic plot of the interaction between a pair of opposite-signed convective columnar vortices at upper layer (top) and lower layer (bottom). The blue curve represents the vorticity profile of a downwelling vortex, which creates a background vorticity field that influences the motion of an adjacent upwelling vortex (denoted by the red circle). Data are for $Ra=3.0\times 10^7$ and $Fr=0.27$.

when $s>l_m$. Since a vortex with positive vorticity moves up a background vorticity gradient, the upwelling vortex undergoes the same translational motions in the upper half layer. As a result, we find $s=l_m$ the most probable radial position where an upwelling vortex locates as shown in figure 9a. For the same reason, one finds most probably a downwelling vortex at a radial distance $s=cr_c$ from an upwelling vortex center (with r_c being the radius of the upwelling vortex). Therefore, we conclude that two opposite-signed convective columnar vortices have a trend of forming a stable pair and exhibit correlated motions.

6.2. Collective Motion

We observe that densely distributed vortices are organized into clusters and move collectively. To further analyze their collective motion, we calculated the spatial correlation function of vortex velocity fluctuation within a cluster

$C(l) = \sum_{ij} [\vec{u}'_i(\vec{r}_i+l) \cdot \vec{u}'_j(\vec{r}_j)] \delta(l-l_{ij}) / [C_0 \sum_{ij} \delta(l-l_{ij})]$, where $\vec{u}'_i = \vec{u}_i - \vec{V}$ is the relative vortex velocity with respect to the mean cluster velocity $\vec{V} = \sum_i \vec{u}_i / N$, l_{ij} is the distance between the vortex pair (i, j) and C_0 is a normalization constant. $\delta(l-l_{ij})$ is a Dirac function selecting pairs of vortices separated by distance l . Figure 10a shows that $C(l)$ decreases as the distance l increases, with a larger decay length for larger clusters. Figure 10b presents the correlation function $C(l/L)$ as a function of l scaled by the cluster length L for $Ra=3.0\times 10^7$ and $Ra/Ra_c=1.97$. We see that for clusters with various sizes N , $C(l/L)$ collapses approximately onto a single stretched exponential function

$$C(l/L) = 1.45e^{(-l/L/0.245)^{0.85}} - 0.45, \quad (6.1)$$

which crosses zero at the correlation length $l_c \approx 0.3L$ for all cluster sizes.

Results of l_c/L are shown as a function of Ra/Ra_c in figure 11 for various Ra . We see indeed over the parameter range studied $l_c/L=0.28\pm 0.03$ remains a constant independent of Ra and Ra/Ra_c . Since l_c represents the characteristic spatial range in which the vortex movements remain correlated, the fact that l_c/L is significantly larger than individual

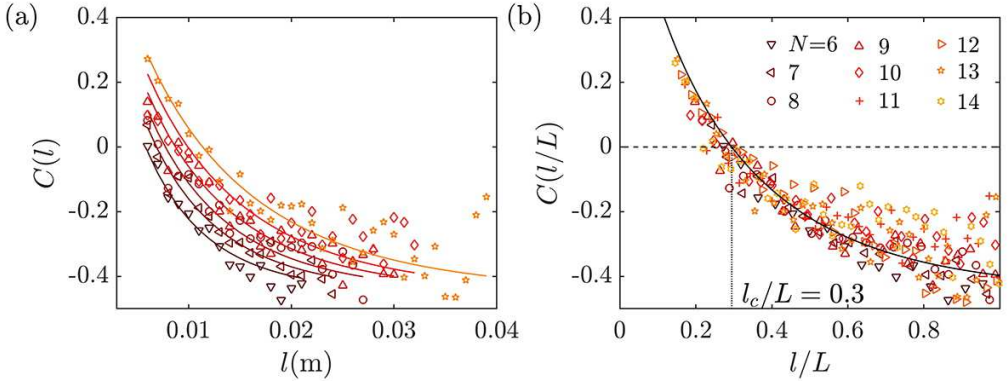


Figure 10: (a) The spatial correlation function of vortex velocity fluctuation within a cluster $C(l)$ as a function of vortex distance l . The solid curves represent the fitted curves $C(l) = (1.45)e^{(-l/H/c)^{0.85}} - 0.45$. The fitted parameter c for various N is ($c=0.077$, $N=6$), ($c=0.091$, $N=7$), ($c=0.100$, $N=8$), ($c=0.115$, $N=9$), ($c=0.131$, $N=10$) and ($c=0.150$, $N=13$). Data of $C(l)$ for larger N appear more scattered about the fitted curve. (b) The correlation function $C(l/L)$ as a function of l/L . The vertical dashed line indicates the correlation length $l_c \approx 0.3L$ determined by the zero-crossing position of $C(l/L)$. Data are for $Ra = 3.0 \times 10^7$ and $Ra/Ra_c = 1.97$.

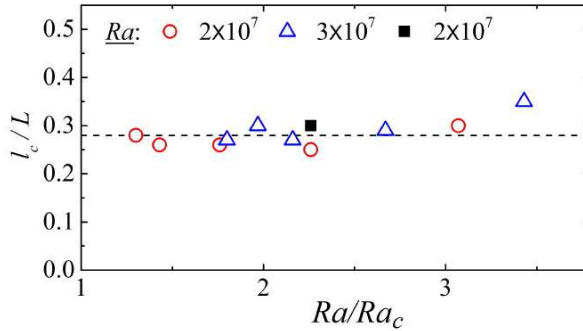


Figure 11: Plot of l_c/L versus Ra/Ra_c for various Ra numbers. Open circles: experimental data for $Ra = 2.0 \times 10^7$. Open triangles: experimental data for $Ra = 3.0 \times 10^7$. Solid squares: numerical data for $Ra = 2.0 \times 10^7$. The dashed line shows the mean value $\langle l_c/L \rangle = 0.28$ for all data

vortex size and independent of the cluster size suggest that the correlated motions of the vortices are long-range and scale-free. Scale-free collective behaviors are also observed in many non-equilibrium dynamical systems consisting of densely distributed, interacting entities, e.g. bird flocks, bacteria swarms and active matters (Cavagna *et al.* 2010; Chen *et al.* 2012; Wysocki *et al.* 2014). For instances, Cavagna *et al.* (2010) observed scale-invariant, correlated motions in starling flocks. Chen *et al.* (2012) found that the correlation length of bacterial motion in clusters is approximately 30% of the spatial size of the clusters. The appearance of scale-free motion of densely populated vortices reported in rapidly rotating convection suggests that it is a general statistical property of collective motion. We remark that the scattering of data points at large distances ($l \approx L$) in figure 10b, owing to insufficient statistics, has negligible influence in the determination of l_c .

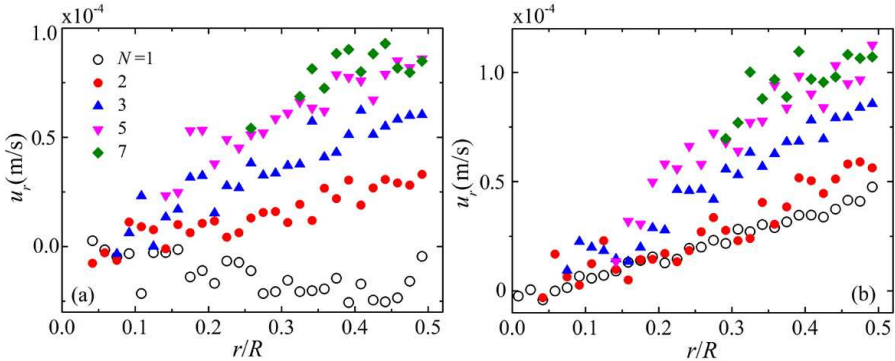


Figure 12: Ensemble-averaged radial velocity $\langle u_r \rangle_\xi$ of the vortices as a function of r/R for various cluster sizes N . Data are for cyclones (a) and anticyclones (b). Results for $Ra=2.0 \times 10^7$ and $Ra/Ra_c=2.26$.

6.3. Centrifugal Motion of Clustered Vortices

We have shown that it is the interaction between adjacent opposite-sign vortices that organizes individual vortices to form vortex clusters. Within each vortex cluster, the translational motion of the vortices are closely correlated and restricted with each other. In the following we make comparative studies of the radial motions of clustered vortices (inside clusters) and isolated vortices (outside clusters).

Figure 12 shows the ensemble-averaged radial velocity $\langle u_r \rangle_\xi$ for the vortices in clusters with various size N . For isolated cyclones that moves individually (i.e., $N=1$), $\langle u_r \rangle_\xi$ is negative and its magnitude increases approximately linearly with r , indicating the normal inward motion of cyclones. However, for clustered cyclones ($N \geq 2$), $\langle u_r \rangle_\xi$ becomes positive which implies anomalous outward motion. We see that the slope of $\langle u_r \rangle_\xi(r)$ increases when N increases up to 5. Therefore, clustered cyclones gain larger velocity of inverse centrifugal motion when the cluster size increases. The velocity profile of anticyclones exhibits a similar cluster-size dependence as the cyclones, except that for $N=1$ $\langle u_r \rangle_\xi(r)$ is positive since isolated anticyclones move outwardly.

We determine the slope λ_u of the velocity profile, through linear fitting of the data $\langle u_r \rangle_\xi$ in the region ($0 \leq r \leq 0.5R$). Results of λ_u as a function of cluster size N for $Ra/Ra_c=2.67$ are shown in figure 13a. We see clearly that in this inverse-centrifugal regime λ_u for cyclones changes sign when N exceeds one. Data for both types of vortices suggest a similar trend for $N \geq 2$, i. e., λ_u increases with N for small cluster sizes and reaches a maximum at $N=5$. We also note that for small cluster size λ_u is considerably larger for anticyclones than cyclones.

When vortices inside a cluster move collectively, they share a similar radial velocity profile $\langle u_r \rangle_\xi(r)$. It is thus reasonable to consider all vortices inside the cluster as a single structure that undergoes radial motion driven by the centrifugal force. We propose a Langevin-type equation analogous to (4.3) to describe, to some extent, the radial motion of vortex clusters, whereby the relaxation time $t_c=M/\eta$ for cluster motion is given by the inertia mass M of all vortices inside the cluster, and ζr defines the net centrifugal force for all vortices. Since in the inverse-centrifugal regime both the population and vorticity strength of anticyclones overrides that of cyclones, the net centrifugal force is positive and thus the vortex cluster moves outwardly. The solution of the radial velocity profile can be obtained through similar a derivation presented in section 4.2, which has the same form as equation (4.5). For a given initial position of the cluster, one finds $\langle u_r \rangle_\xi = \lambda_u r$ with the mobility

$$\lambda_u = \sqrt{1/(4t_c^2) + \zeta} - 1/(2t_c).$$

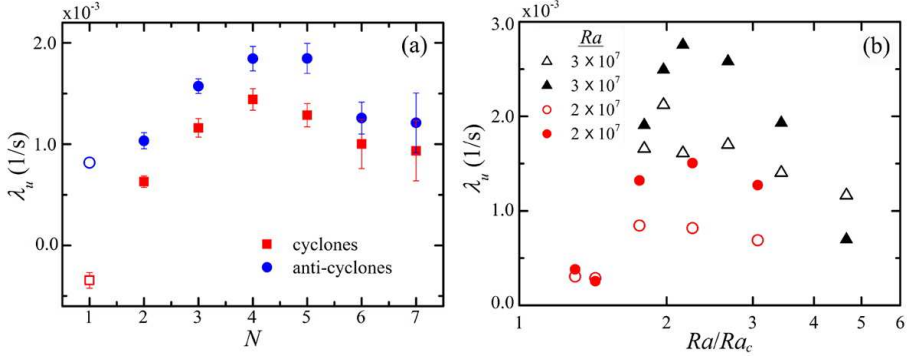


Figure 13: Mobility λ_u of vortex motion determined from the slope of $\langle u_r \rangle_\xi(r)$. (a) λ_u as a function of N for $Ra=2.0 \times 10^7$ and $Ra/Ra_c=2.26$. (b) λ_u as a function of Ra/Ra_c for various Ra . Open symbols are data for isolated anticyclones ($N=1$). Solid symbols are data for clustered anticyclones ($N>1$).

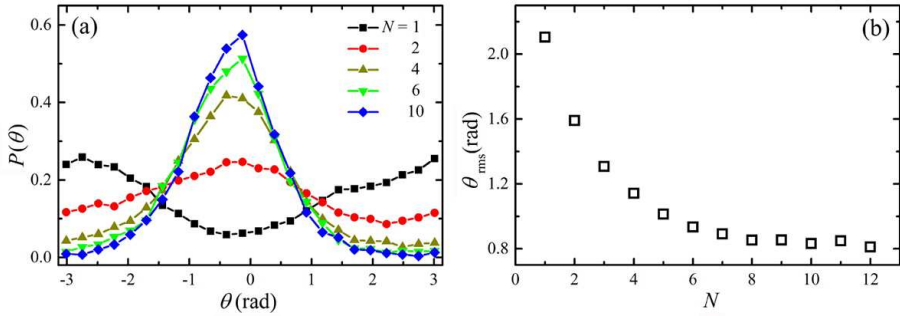


Figure 14: (a) Probability density functions of θ of cyclones in clusters with various size N . (b) The standard deviation of θ as a function of the cluster size N . Results for $Ra=3.0 \times 10^7$, $Ra/Ra_c=1.97$ and $Fr=0.27$

As shown in figure 13a the mobility of clusters λ_u is in the order of 10^{-3} (1/s) , and $t_c \approx 10s$ in the inverse-centrifugal regime (see Ding *et al.* 2021), we find $1/(2t_c) \gg \lambda_u$, $\zeta \ll 1/(2t_c)^2$ and thus $\lambda_u \approx \zeta t_c = \Omega^2 \langle \delta T \rangle t_c = \Omega^2 \langle \delta T \rangle M / \eta$. Here $\langle \delta T \rangle$ is the averaged temperature anomaly of the vortex cluster. With increasing cluster size N , the inertia mass M of the cluster increases. We suggest that it is the dominating factor for an enlarged λ_u for clusters of intermediate size ($N \approx 5$). For very large cluster size ($N \geq 5$) we infer that viscous damping may become significant to influence cluster motion and thereby λ_u decreases.

Figure 13b presents λ_u as a function of Ra/Ra_c for isolated ($N=1$, open symbols) and clustered ($N>1$, solid symbols) anticyclones. Data for two sets of Ra are shown for comparisons. One sees that for a given Ra and Ra/Ra_c , λ_u is greater for clustered anticyclones than for isolated anticyclones. For all cases λ_u has a maximum at $Ra/Ra_c \approx 2$. We see that the maximum λ_u for clustered anticyclones is nearly twice that of the isolated ones for both Ra numbers. We also see that λ_u increases further when a larger Ra is chosen. These results demonstrate that the radial motion of anticyclones are enhanced by the collective motion to a great extent.

We further investigate the direction of motion \hat{u} of cyclones. Denoting the angle θ between \hat{u} and the vortex position \hat{r} , we show in figure 14a the probability density function $p(\theta)$ for cyclones in clusters with various sizes. We find that θ depends strongly on the cluster size N . For isolated cyclones ($N=1$), the most probable direction of motion is radially inward

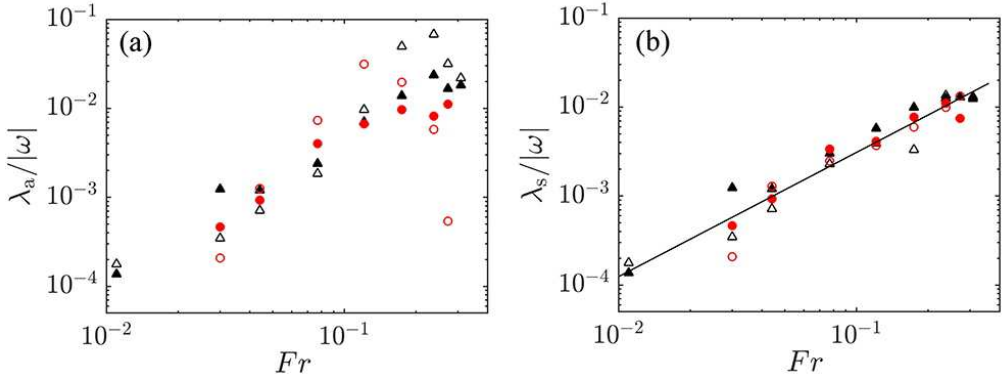


Figure 15: (a) The mobility $\lambda_a/|\omega|$ of all vortices scaled by the vorticity magnitude as a function of Fr . (b) The scaled mobility $\lambda_s/|\omega|$ of isolated vortices as a function of Fr . Results are for $Ra=2.0 \times 10^7$ (red circles) and $Ra=3.0 \times 10^7$ (black triangles). Open symbols: cyclones. Solid symbols: anticyclones. The solid line represents a power-function fit with an exponent of 1.40 ± 0.13 .

($\theta_p = \pi$). However, for clustered cyclones ($N \geq 2$) we find $\theta_p = 0$ as they move outward. For small cluster size θ is widely distributed and thus $p(\theta)$ exhibits a broad half width. When the cluster size increases we find the distribution of θ becomes concentrated around $\theta_p = 0$ with increasing maximum of $P(\theta)$. Figure 14b shows that the standard deviation of θ indeed decreases monotonically when N increases. With increasing cluster size N the inertial effect of the vortex cluster becomes significant. Our data reveal that the inverse centrifugal motion of cyclones appears more unidirectional.

6.4. Froude-number Dependence of the Vortex Mobility

The mobility λ_u represents the primary features of radial motion for both isolated and clustered vortices. We suggest that the non-monotonic dependence of λ_u on Ra/Ra_c shown in figure 13b is thus owing to the decreasing vorticity magnitude $|\omega|$ that competes with the increasing rotation rate Ω . Following discussions in sections 4.2 and 6.3, we have $\lambda_u \approx \zeta t_c = \Omega^2 \delta T m / \eta$. The temperature anomaly δT of the convective vortices represents the buoyancy forcing, which is predicted to be proportional to the vorticity magnitude of the vortices (Portegies *et al.* 2008; Grooms *et al.* 2010). Thus the mobility of clusters can approximate to $\lambda_u \approx c^*(z) \Omega^2 |\omega| m / \eta$, with the coefficient $c^*(z)$ depending on the fluid depth. This approximate relation implies that the mobility of the vortices is determined not only by the rotating rate but also the vorticity magnitude of the vortices. In figure 15a we show the scaled mobility $\lambda_a/|\omega|$ as a function of Fr for both types of vortices. Here λ_a is determined by linear fitting of the radial velocity profile $\langle u_r \rangle_\xi(r)$ shown in figures 12 and 13 for both isolated ($N=1$) and clustered vortices ($N>1$). Since $\lambda_a/|\omega| = c^*(z) \Omega^2 m / \eta$, the scaled mobility is expected to increase when the rotation rate increases. Our experimental results in figure 15a show that it is the case as $\lambda_a/|\omega|$ for both cyclones and anticyclones grows rapidly with increasing Fr in the full parameter range studied. Meanwhile we see that results for $\lambda_a/|\omega|$ are scattered and there exists notable difference between the cyclonic and anticyclonic data for given Fr and Ra .

We suggest that the vortex-interaction of vortices forming clusters may disturb individual vortex motion and modify the vortex mobility. In supporting this argument, we determine the mobility λ_s for isolated vortices, calculating the slope of the velocity profile $\langle u_r \rangle_\xi(r)$ (e. g. shown in figure 13) for both cyclones and anticyclones for the case of $N=1$. Results of

$\lambda_s/|\omega|$ are shown as a function of Fr in figure 15b. We see that the discrepancy of $\lambda_s/|\omega|$ between isolated cyclones and anticyclones is minor. Moreover, data of $\lambda_s/|\omega|$ for various Ra collapse onto a power-law function $\lambda_s/|\omega| \propto Fr^{1.40 \pm 0.13}$ in the full parameter range of Fr studied, suggesting a general scaling relationship. These results imply that the mobility of isolated vortices scaled by the magnitude of their vorticity can be adequately determined by the Froude number.

7. Summary and Discussions

A major emphasis of previous studies in rotating convection has been on the flow structures of the columnar vortices (Vorobieff & Ecke 2002; Sprague *et al.* 2006; Portegies *et al.* 2008; Grooms *et al.* 2010; Nieves *et al.* 2014; Rajaei *et al.* 2017; Shi *et al.* 2020). As reported briefly in earlier works, these columnar vortices exhibit intriguing translational horizontal motions (Sakai 1997; King & Aurnou 2012; Noto *et al.* 2019; Chong *et al.* 2020; Ding *et al.* 2021). We present here experimental and numerical studies of the vortex dynamics in rotating RBC in the parameter range of $2.0 \times 10^7 \leq Ra \leq 2.7 \times 10^8$, $1.7 \times 10^{-5} \leq Ek \leq 2.7 \times 10^{-4}$ and $0 \leq Fr \leq 0.31$, which covers the four flow regimes of vortex motion, (I) random vortex diffusion, (II) centrifugal-forced diffusion, (III) inverse-centrifugal motion and (IV) asymptotic centrifugal motion. We found that under slow rotations with $Ra \geq 10Ra_c$, the vortices undergo Brownian-type random motion, i.e., the MSD of the vortices first increases in time as t^2 in the ballistic regime, and then linearly in the diffusive regime. Our close inspection of the PDFs of the vortex displacements reveal that, however, the diffusive motion of the vortices is non-Gaussian at small time intervals. Furthermore, we show that in this weakly rotating convection state, the vortices are randomly distributed over the horizontal plane, with the PDFs of the Voronoi cell areas of the vortices well described by the standard Γ distribution.

With modest strength of rotations the centrifugal force influences the dynamics of the columnar vortices. We observed that in this flow regime, cyclones move radially towards the rotation axis while anticyclones migrate outwards. Such radial motions of the vortices lead to their super-diffusive behavior, i. e. , the MSD of the vortices increases faster than a linear function of time at large time. Space-time plots of the radial trajectories of the vortices suggest that despite their significant fluctuations, the mean radial displacements of the vortices follow approximately exponential functions of time. Moreover, we note that the ensemble-averaged of the radial velocity $\langle u_r \rangle_\xi$ of cyclones (anticyclones) is negative (positive) and increases (decreases) linearly with respect to r . Based on these observations, we proposed an extended Langevin model incorporating the centrifugal force to interpret the vortex motion in the centrifugation-influenced flow regime. The model provides predictions of the first and second moments of the radial displacements of both types of the vortices which coincide with the experimental data, and explains the linear radial dependence of $\langle u_r \rangle_\xi$. Our model thus presents essential interpretations of the super-diffusive behavior of the horizontal vortex motion observed in rotating convection systems (Noto *et al.* 2019; Ding *et al.* 2021).

With increasing rotation speed the horizontal scale of the columnar vortices decreases. It is found that the mean area of the Voronoi cells of the vortices decreases significantly in the flow regime with $1.6Ra_c \leq Ra \leq 4Ra_c$, signifying that the vortices are densely distributed. The PDFs of the Voronoi cell area deviate markedly from the standard Γ distribution. In this convection state, the hydrodynamic interaction of neighboring vortices becomes prominent to influence the vortex dynamics. We report the existence of a most probable separation between two adjacent counter-rotating vortices that tends to form a vortex pair and move collectively. Such vortex interactions eventually lead to the formation of large-scale vortex clusters. We show that inside the clusters the vortices exhibit correlated motion. The correlation of the

translation velocity fluctuations of the vortices is scale invariant, with the correlation length being approximately 30% of the length scale of the clusters. In this centrifugation-dominated flow regime, the cold anticyclones override the warm cyclones both in vorticity strength and population, a flow-field asymmetry brought about by the centrifugal effect. Within vortex clusters the motion of the weak cyclones thus submit to that of strong anticyclones and move outwardly in a collective manner. We suggest that this is the underlying mechanism for the counterintuitive inverse-centrifugal motion of the cyclones.

Within each vortex clusters, the translational motion of the vortices are long-range correlated. We show that such correlated motion of the clustered vortices exerts essential influences on their dynamics. With increasing cluster size N , the radial velocity $\langle u_r \rangle_\xi(r)$ for clustered cyclones and anticyclones increases faster with r , thus both types of vortices gain a larger translation velocity moving outwardly. We also note that the translational motion of cyclones in larger clusters is more concentrated in the outward direction, indicating that their inverse centrifugal motion becomes more unidirectional. Finally, despite the complicated Fr -dependence of the scale vortex mobility $\lambda_a/|\omega|$ for all vortices, we discover in the full parameter range of Fr a simple power-law scaling $\lambda_s/|\omega| \propto Fr^{1.4}$ for isolated vortices for various Ra and vortex types.

We have shown in this work the rich and intriguing vortex dynamics in rotating RBC. There remain numerous issues requiring further investigations. Prominent among those include the origin of the Brownian but non-Gaussian diffusion of the vortex displacements. Such non-Gaussian diffusive motion becomes apparent at short time scales. Another crucial issue awaiting theoretical descriptions is the hydrodynamic interactions among closely located convective vortices that give rise to the long-range collective motion of the vortices. Equally important would be explanations of the scale-free correlation of the vortex velocity fluctuations that exist in large-scale vortex clusters. What are the implications of the vortex dynamics presented in this study for the correlated vortex motion observed in giant gaseous planets and other large-scale geophysical and astrophysical flows (Li *et al.* 2020; Mura *et al.* 2021; Gavriel & Kaspi 2021, 2022)? We expect future progress in answering these questions.

Acknowledgements. This work is supported by the National Science Foundation of China under Grant No. 92152105, 12232010 and 12072144, a NSFC/RGC Joint Research Grant No. 11561161004 (JQZ) and N_CUHK437/15 (KQX) and by the Hong Kong Research Grants Council under Grant No. 14301115 and 14302317. JQZ acknowledges the support from the Research Program of Science and Technology Commission of Shanghai Municipality.

Author contributions. J.-Q.Z. and K.-Q.X. conceived and designed research. S.-S.D. and W.-T.W. conducted the experiments. G.-Y.D. and K.L.C. conducted the numerical simulations. S.-S.D., J.-Q.Z. and K.-Q.X. wrote the manuscript.

Declaration of interests. The authors report no conflict of interest.

REFERENCES

- AURNOU, J. M., BERTIN, V. & GRANNAN, A. M. 2018 Rotating thermal convection in liquid gallium: multi-modal flow, absent steady columns. *J. Fluid Mech.* **846**, 846–876.
- BOUBNOV, B. M. & GOLITSYN, G. S. 1986 Experimental study of convective structures in rotating fluids. *J. Fluid Mech.* **167**, 503–531.
- CAVAGNA, A., CIMARELLI, A., GIARDINA, I., PARISI, G., SANTAGATI, R., STEFANINI, F. & VIALE, M. 2010 Scale-free correlations in starling flocks. *Proc. Natl. Acad. Sci. U. S. A.* **107** (26), 11865.
- CHANDRASEKHAR, S. 1961 *Hydrodynamic and Hydromagnetic Stability*. Oxford: Oxford University Press.
- CHEN, X., DONG, X., BE'ER, A., SWINNEY, H. L. & ZHANG, H. P. 2012 Scale-invariant correlations in dynamic bacterial clusters. *Phys. Rev. Lett* **108** (14), 148101.
- CHONG, K. L., DING, G. & XIA, K.-Q. 2018 Multiple-resolution scheme in finite-volume code for active or passive scalar turbulence. *J. Comp. Phys.* **375**, 1045–1058.

- CHONG, K. L., SHI, J.-Q., DING, S.-S., DING, G.-Y., LU, H.-Y., ZHONG, J.-Q. & XIA, K.-Q. 2020 Vortices as Brownian particles in turbulent flows. *Sci. Adv.* **6**, eaaz1110.
- DING, S.-S., CHONG, K. L., SHI, J.-Q., DING, G.-Y., LU, H.-Y., XIA, K.-Q. & ZHONG, J.-Q. 2021 Inverse centrifugal effect induced by collective motion of vortices in rotating turbulent convection. *Nat. Commun.* **12**, 5585.
- DING, S.-S., ZHANG, H.-L., CHEN, D.-T. & ZHONG, J.-Q. 2022 Vortex patterns in rapidly rotating Rayleigh-Bénard convection under spatial periodic forcing. *J. Fluid Mech.* **950**, R1.
- FERNANDO, H. J. S. & SMITH, D. C. 2001 Vortex structures in geophysical convection. *Eur. J. Mech. B - Fluids* **20**, 437–470.
- FUJITA, K., TASAKA, Y., YANAGISAWA, T., NOTO, D. & MURAI, Y. 2020 Three-dimensional visualization of columnar vortices in rotating rayleigh-bénard convection. *J. Visualization* **24**, 635–647.
- GAVRIEL, N. & KASPI, Y. 2021 The number and location of jupiter's circumpolar cyclones explained by vorticity dynamics. *Nat. Geosci.* **14**, 559–563.
- GAVRIEL, N. & KASPI, Y. 2022 The oscillatory motion of jupiter's polar cyclones results from vorticity dynamics. *Geophys. Res. Lett.* **49**, e2022GL098708.
- GROOMS, I., JULIEN, K., WEISS, J. B. & KNOBLOCH, E. 2010 Model of convective Taylor columns in rotating Rayleigh-Bénard convection. *Phys. Rev. Letts.* **104**, 224501.
- HART, J. E. & OLSEN, D. R. 1999 On the thermal offset in turbulent rotating convection. *Phys. Fluids* **11**, 2101–2107.
- HOPFINGER, E. J. & VAN HEIJST, G. J. F. 1993 Vortices in rotating fluids. *Annu. Rev. Fluid Mech.* **25**, 241–89.
- HORN, S. & AURNOU, J. M. 2018 Regimes of coriolis-centrifugal convection. *Phys. Rev. Letts.* **120**, 204502.
- HORN, S. & AURNOU, J. M. 2019 Rotating convection with centrifugal buoyancy: Numerical predictions for laboratory experiments. *Phys. Rev. Fluids* **4**, 073501.
- HU, Y.-B., HUANG, S.-D., XIE, Y.-C. & XIA, K.-Q. 2021 Centrifugal-force-induced flow bifurcations in turbulent thermal convection. *Phys. Rev. Letts.* **127**, 244501.
- HU, Y.-B., XIE, Y.-C. & XIA, K.-Q. 2022 On the centrifugal effect in turbulent rotating thermal convection: onset and heat transport. *J. Fluid Mech.* **938**, R1.
- JONES, C. A. 2011 Planetary magnetic fields and fluid dynamos. *Annu. Rev. Fluid Mech.* **43**, 583–614.
- JULIEN, K. & KNOBLOCH, E. 1998 Strongly nonlinear convection cells in a rapidly rotating fluid layer: the tilted f -plane. *J. Fluid Mech.* **360**, 141–178.
- JULIEN, K., LEGG, S., MCWILLIAMS, J. & WERNE, J. 1996 Rapidly rotating Rayleigh-Bénard convection. *J. Fluid Mech.* **322**, 243–273.
- JULIEN, K., RUBIO, A. M., GROOMS, I. & KNOBLOCH, E. 2012 Statistical and physical balances in low rossby number Rayleigh-Bénard convection. *Geophys. Astrophys. Fluid. Dyn.* **106**, 392–428.
- KACZOROWSKI, M. & XIA, K.-Q. 2013 Turbulent flow in the bulk of Rayleigh-Bénard convection: small-scale properties in a cubic cell. *J. Fluid Mech.* **722**, 596–617.
- KING, E. M. & AURNOU, J. M. 2012 Thermal evidence for Taylor columns in turbulent rotating Rayleigh-Bénard convection. *Phys. Rev. E* **85**, 016313.
- KING, E. M., STELLMACH, S., NOIR, J., HANSEN, U. & AURNOU, J. M. 2009 Boundary layer control of rotating convection systems. *Nature* **457**, 301.
- KUNDU, P. K. & COHEN, I. M. 2008 *Fluid Mechanics*. Burlington: Academic Press.
- KUNNEN, R. P. J., CLERCX, H. J. H. & GEURTS, B. J. 2010 Vortex statistics in turbulent rotating convection. *Phys. Rev. E* **82**, 036306.
- LI, C., INGERSOLL, A. P., KLIPFEL, A. P. & BRETTLE, H. 2020 Modeling the stability of polygonal patterns of vortices at the poles of jupiter as revealed by the juno spacecraft. *Proc. Natl. Acad. Sci.* **117**, 24082–24087.
- LIU, Y. & ECKE, R. E. 2011 Local temperature measurements in turbulent rotating Rayleigh-Bénard convection. *Phys. Rev. E* **84**, 016311.
- MARSCHALL, J. & SCOTT, F. 1999 Open-ocean convection: Observations, theory and models. *Rev. Geophys.* **37**, 1–64.
- MURA, A., ADRIANI, A., BRACCO, A., MORICONI, M. L., GRASSI, D., PLAINAKI, C. & ET AL. 2021 Oscillations and stability of the jupiter polar cyclones. *Geophys. Res. Lett.* **48**, e2021GL094235.
- NIEVES, D., RUBIO, A. M. & JULIEN, K. 2014 Statistical classification of flow morphology in rapidly rotating Rayleigh-Bénard convection. *Phys. Fluids* **26**, 086602.
- NOTO, D., TASAKA, Y., YANAGISAWA, T. & MURAI, Y. 2019 Horizontal diffusive motion of columnar vortices in rotating Rayleigh-Bénard convection. *J. Fluid Mech.* **871**, 401.

- PORTEGIES, J. W., KUNNEN, R. P. J., VAN HEIJST, G. J. F. & MOLENAAR, J. 2008 A model for vortical plumes in rotating convection. *Phys. Fluids* **20**, 066602.
- RAJAEI, H., KUNNEN, R. P. J. & CLERCX, H. J. H. 2017 Exploring the geostrophic regime of rapidly rotating convection with experiments. *Phys. Fluids* **20**, 045105.
- SAKAI, S. 1997 The horizontal scale of rotating convection in the geostrophic regime. *J. Fluid Mech.* **333**, 85–95.
- SCHECTER, D. A. & DUBIN, D. H. 1999 Vortex motion driven by a background vorticity gradient. *Phys. Rev. Letts.* **83**, 2191–2194.
- SHI, J.-Q., LU, H.-Y., DING, S.-S. & ZHONG, J.-Q. 2020 Fine vortex structure and flow transition to the geostrophic regime in rotating Rayleigh-Bénard convection. *Phys. Rev. Fluids* **5**, 011501(R).
- SPRAGUE, M., JULIEN, K., KNOBLOCH, E. & WERNE, J. 2006 Numerical simulation of an asymptotically reduced system for rotationally constrained convection. *J. Fluid Mech.* **551**, 141–174.
- STELLMACH, S., LISCHPER, M., JULIEN, K., VASIL, G., CHENG, J. S., RIBEIRO, A., KING, E. M. & AURNOU, J. M. 2014 Approaching the asymptotic regime of rapidly rotating convection: Boundary layers versus interior dynamics. *Phys. Rev. Letts.* **113**, 254501.
- VALLIS, G. K. 2006 *Atmospheric and Oceanic Fluid Dynamics*. Cambridge: Cambridge University Press.
- VOROBIEFF, P. & ECKE, R. E. 1998 Vortex structure in rotating rayleigh-bénard convection. *J. Fluid Mech.* **123**, 156–160.
- VOROBIEFF, P. & ECKE, R. E. 2002 Turbulent rotating convection: an experimental study. *J. Fluid Mech.* **458**, 191–218.
- WESTERWEEL, J., ELSINGA, G. E. & ADRIAN, R. J. 2013 Particle image velocimetry for complex and turbulent flows. *Annu. Rev. Fluid Mech.* **45**, 409–36.
- DE WIT, X. M., AGUIRRE GUZMÁN, A. J., MADONIA, M., CHENG, J. S., CLERCX, H. J. H. & KUNNEN, R. P. J. 2020 Turbulent rotating convection confined in a slender cylinder: The sidewall circulation. *Phys. Rev. Fluids* **5**, 023502.
- WYSOCKI, A., WINKLER, R. G. & GOMPPER, G. 2014 Cooperative motion of active brownian spheres in three-dimensional dense suspensions. *Europhys. Lett.* **105**, 48004.
- ZHANG, X., VAN GILS, D. P. M., HORN, S., WEDI, M., ZWIRNER, L., AHLERS, G., ECKE, R. E., WEISS, S., BODENSCHATZ, E. & SHISHKINA, O. 2020 Boundary zonal flow in rotating turbulent Rayleigh-Bénard convection. *Phys. Rev. Lett.* **124**, 084505.
- ZHONG, F., ECKE, R. & STEINBERG, V. 1993 Rotating Rayleigh-Bénard convection: asymmetric modes and vortex states. *J. Fluid Mech.* **249**, 135.